Supporting Information

Sn-doped Bi_2O_3 Nanosheets for Highly Efficient Electrochemical CO_2 Reduction toward Formate Production

Xiao Li,[a] Xingqiao Wu,[a] Junjie Li,[a] Jingbo Huang,[a] Liang Ji,[a] Zihan Leng,[a] Ningkang Qian,[a] Deren Yang,[a] Hui Zhang,[a,b,*]

[a]*State Key Laboratory of Silicon Materials and School of Materials Science and Engineering, Zhejiang University, Hangzhou, Zhejiang 310027, People's Republic of China.*

[b]*Institute of Advanced Semiconductors, Hangzhou Innovation Center, Zhejiang University, Hangzhou, Zhejiang 310027, People's Republic of China.*

Corresponding to msezhanghui@zju.edu.cn

Experimental section

Chemicals

Bismuth (III) nitrate pentahydrate ($Bi(NO_3)_3 \cdot 5H_2O$, 98%) and Tin(II) chloride dihydrate ($SnCl_2 \cdot 2H_2O$, 98%) were both purchased from Sigma Aldrich. Potassium bicarbonate ($KHCO_3$, 99.9%) were bought from Macklin Biochemical Co., Ltd. Ethanol and ethylene glycol were purchased from Sinopharm Chemical Reagent Co., Ltd. Ultra-pure deionized water (18.2 MΩ·cm) were used in all the aqueous experiments. All the reagents were used without additional purification.

Synthesis of Sn-doped Bi_2O_3 NSs

Sn-doped Bi_2O_3 NSs were synthesized in polyol by a solvothermal method. In a typical procedure, 680 mg of $Bi(NO_3)_3 \cdot 5H_2O$ and different amounts of $SnCl_2 \cdot 2H_2O$ (i.e., 7.9, 15.8, and 31.6 mg) were dissolved in a mixture of 24 mL of ethanol, 12 mL of ethylene glycol and 4 mL of deionized water, and then sonicated for 30 min. Subsequently, the obtained transparent solution was sealed in a 55 mL Teflon-lined stainless-steel autoclave and heated in an oven at 160 °C for 5 h. After that, the product was centrifuged and washed with ethanol and deionized water for three times. Finally, Sn-doped Bi_2O_3 NSs were obtained after freeze-drying.

Synthesis of undoped Bi_2O_3 Nanosheets

The Bi_2O_3 NSs were prepared by the similar procedure as Sn-doped Bi_2O_3 NSs, except for the absence of $SnCl_2 \cdot 2H_2O$ in the synthesis.

Characterizations of Materials

Transmission electron microscopy (TEM) images were taken on a Hitachi HT-7700 microscope at an operating voltage of 100 kV. A FEI Tecnai G2 F20 microscope was employed to achieve

high-resolution (TEM) images operated at 200 kV accelerating voltage. High-angle annular dark-field scanning TEM (HAADF-STEM) images were obtained through a FEI Titan ChemiSTEM operated at 200 kV. The X-ray diffraction (XRD) characterization was performed on the X-ray diffractometer (Rigaku D/max-ga) with Cu Kα radiation (graphite monochromatized, λ = 1.541 Å). X-ray photoelectron spectrometer (XPS) analysis was carried out on a scanning X-ray microprobe (Axis Supra, Kratos Inc.) with Al Kα radiation. The corresponding binding energies were calibrated with C-C 1s peak (284.8 eV). The atomic ratio of Bi and Sn in the samples were achieved by inductively coupled plasma atomic emission spectrometry (ICP-AES, IRIS Intrepid II XSP, TJA Co.). CO_2 adsorption isotherms were obtained by Micromeritics ASAP 2020M at 25°C. The amount of each sample used in the test is ~200 mg. Before the CO_2 adsorption experiment, two cycles of gas desorption were performed.

Electrochemical measurements

Electrochemical testing was carried out in a home-made H-type two-compartment cells with good air tightness. The cathode compartment housed the working electrode and reference electrode (Ag/AgCl) and the anode compartment housed the counter electrode (Pt plate). To prepare the working electrode, 1 mg of catalyst powder obtained after freeze-drying and 0.5 mg of carbon black (XC-72R) were dispersed in 125 μL of deionized water,125 μL ethanol and 10 μL of 5 wt% Nafion solution, and bath-sonicated for more than 20 min to form a homogeneous ink. The purpose of adding carbon black is to load the dispersed catalysts and enhance their electrical conductivity in the catalytic process. The ink was then uniformly spread on a 1 × 1 cm^2 carbon fiber paper and dried naturally. The two compartments were separated by an anion

exchange membrane and each one was filled with 35 mL of 0.5 M $KHCO_3$ electrolyte. The aforementioned electrolyte was bubbled with CO_2 for 1 h prior to measurements. During the measurements, the electrolyte was continuously bubbled with CO_2 at a flow rate of 20 sccm. In the cathodic compartment, the electrolyte is under stirring with a stir bar at a mild speed. All the potentials mentioned below were converted to RHE using this equation: $E_{RHE} = E_{Ag/AgCl} + 0.197 + 0.0591 \times pH$ without IR compensation. Electroreduction products were qualitatively and quantitatively analyzed using gas chromatography (Agilent, GC7980B) and ion chromatography (Dionex ICS-900). The faradic efficiency (FE) for gas products (H_2 or CO) was calculated as follows:

$$FE_{H_2\ or\ CO}(\%) = \frac{Q_{H_2}}{Q_{total}} \times 100\% = \frac{(\frac{v}{60\ s/min}) \times (\frac{y}{24000 cm^3/mol}) \times N \times F}{i} \times 100\%$$

where v = 20 sccm, which is the CO_2 flow rate, y is the product concentration measured by GC, N = 2 is the number of electron transfer to form a molecule of H_2 or CO, F is the Faraday constant (96485 $C \cdot mol^{-1}$), and i is the total current measured by the electrochemical workstation (CHI760E). The FE for HCOOH in the catholyte was calculated as follows:

$$FE_{HCOO^-}(\%) = \frac{Q_{HCOO^-}}{Q_{total}} \times 100\% = \frac{n_{HCOO^-} \times N \times F}{Q} \times 100\%$$

where n_{HCOO^-} is the amount of formate determined by ion chromatography, and the Q corresponds to the amount of cumulative charge in the process of CO_2 reduction, which was provided by the electrochemical workstation. The energy efficiency (EE) at a certain negative potential for HCOOH generation was calculated as follows:

$$EE = \frac{E_0 \times FE}{E_0 + \eta} \times 100\%$$

Where E_0 (V) is the equilibrium potential; FE (%) is the faradic efficiency for HCOOH generation at the equilibrium potential; η (V) is the overpotential.

The ECSA of all the electrocatalysts is calculated from the electrochemical double-layer capacitance (C_{dl}), which is derived from the cyclic voltammograms (CVs) at a non-Faradaic potential range (0.43 V vs. RHE to 0.53 V vs. RHE). The CV scan rates are from 20 mV/s to 200 mV/s. C_{dl} was the half of the slope in Fig. 4b. Electrochemical impedance spectroscopy (EIS) was recorded at the open circuit voltage in CO_2-saturated 0.5 M $KHCO_3$ electrolyte with an amplitude of 5 mV. The frequency range is from 0.1 Hz to 100000 Hz.

DFT calculation details.

The first-principles calculations were carried out with the Vienna ab initio simulation package[1,2]. The interaction between ions and valence electrons is described using projector augmented wave (PAW) potentials. The exchange-correlation between electrons is treated through using the generalized gradient approximation (GGA) in the Perdew-Burke-Ernzerhof (PBE) form[3]. DFT-D3 method was employed to calculate the van der Waals (vdW) interaction. To achieve the accurate density of the electronic states, the plane wave cutoff energy was 520 eV, a 3× 3×1 for sheet k-point mesh were used. Ionic relaxations were carried out under the conventional energy (10^{-4} eV) and force (0.01 eV/Å) convergence criteria. The Bi_2O_3 slab along the (200) projection was used to mimic the as-prepared (200) lattice plane, in which 1.5 nm vacuum layer was added to avoid the interaction between adjacent layers.

Gibbs free energies for each gaseous and adsorbed species were calculated at 298.15 K, according to the expression:

$$G = E_{DFT} + E_{ZPE} - TS$$

$E_{ZPE} = \sum_i 1/2\ h\nu_i$

$\Theta_i = h\nu_i / k$

$S = \sum_i R[\ln (1-e^{-\Theta i/T})^{-1} + \Theta_i/T\ (e^{\Theta i/T} - 1)^{-1}]$

where E_{DFT} is the electronic energy calculated for specified geometrical structures, E_{ZPE} is the zero-point energy, S is the entropy, h is the Planck constant, ν is the computed vibrational frequencies, Θ is the characteristic temperature of vibration, k is the Boltzmann constant, and R is the molar gas constant. For adsorbates, all 3N degrees of freedom were treated as frustrated harmonic vibrations with negligible contributions from the catalysts' surfaces. In the computational hydrogen electrode (CHE) model,[4] each reaction step was treated as a simultaneous transfer of the proton-electron pair as a function of the applied potential.

The adsorption energy (E_{ads}) of the OCHO was calculated as $E_{ads} = E_{substrate+adsorbate} - E_{substrate} - E_{adsorbate}$.

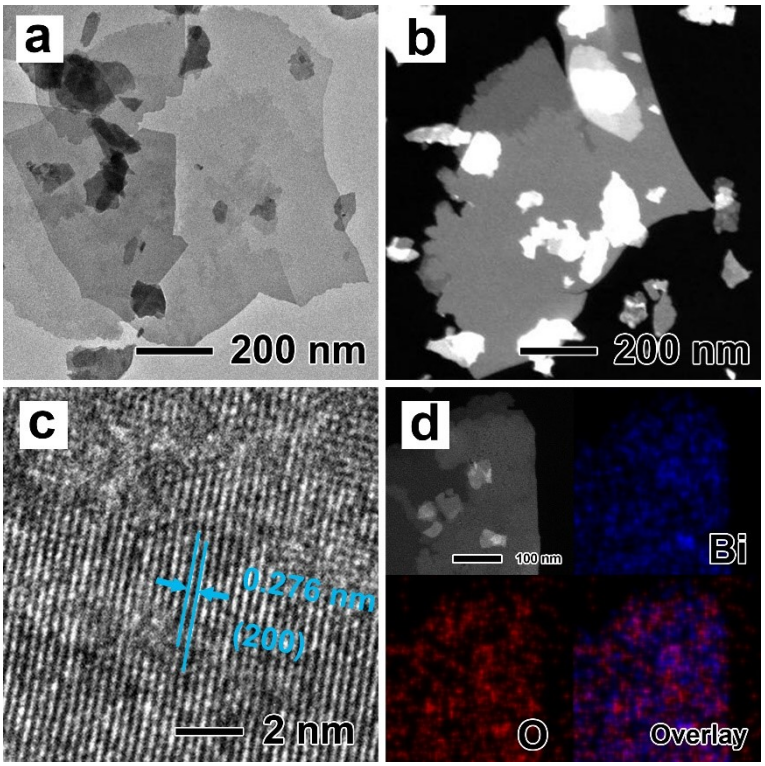

Fig. S1. (a) TEM, (b) HAADF-STEM, (c) HRTEM, and (d) EDX mapping images of undoped Bi_2O_3 NSs.

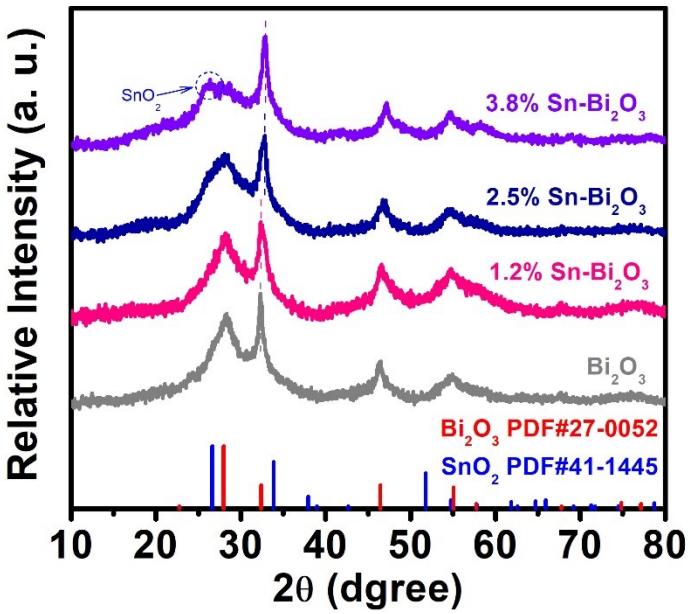

Fig. S2. XRD patterns of undoped Bi_2O_3 NSs, 1.2% Sn-doped Bi_2O_3 NSs, 2.5% Sn-doped Bi_2O_3 NSs and 3.8% Sn-doped Bi_2O_3 NSs.

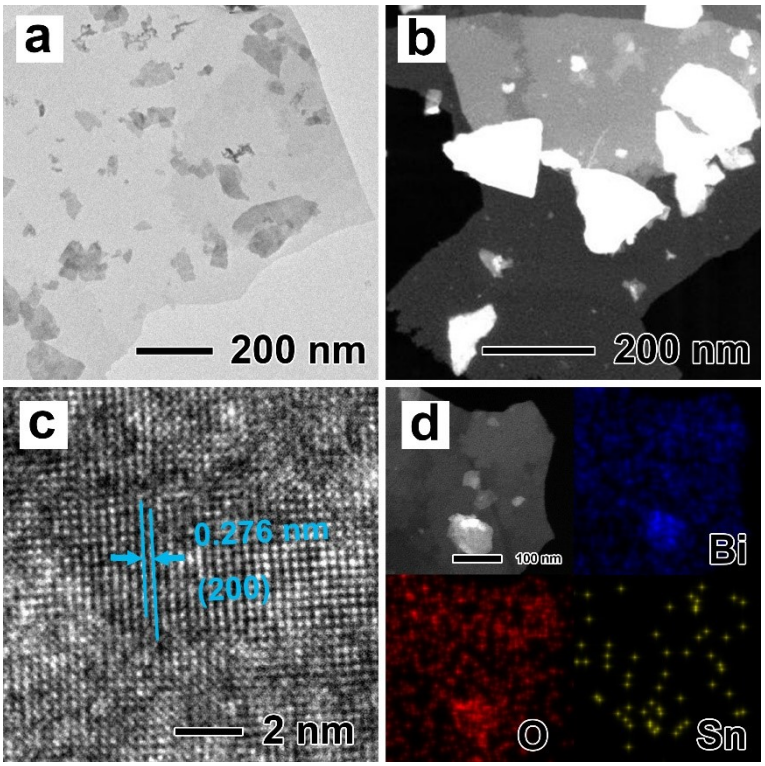

Fig. S3. (a) TEM, (b) HAADF-STEM, (c) HRTEM, and (d) EDX mapping images of 1.2% Sn-doped Bi_2O_3 NSs.

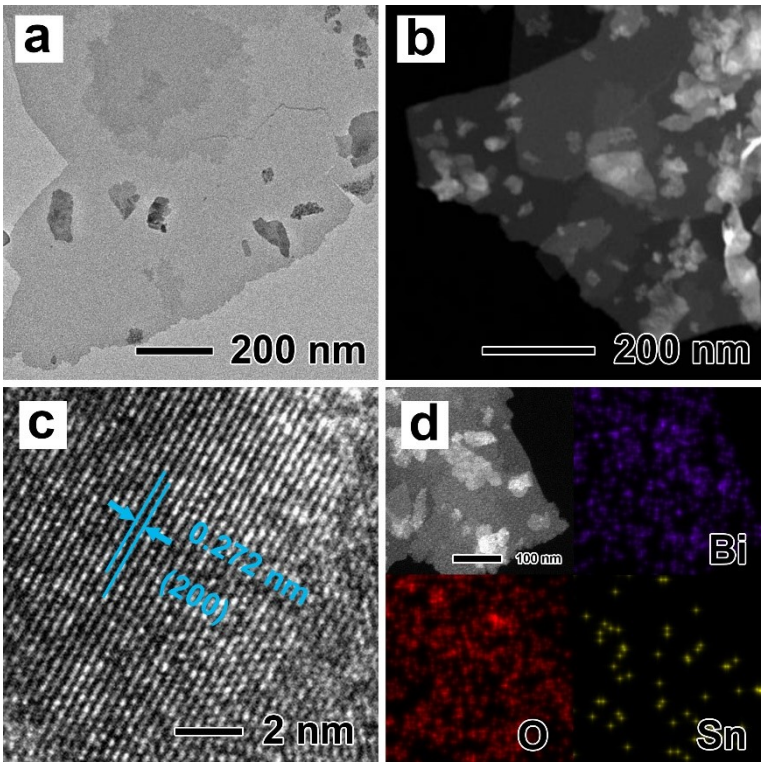

Fig. S4. (a) TEM, (b) HAADF-STEM, (c) HRTEM, and (d) EDX mapping images of 3.8% Sn-doped Bi_2O_3 NSs.

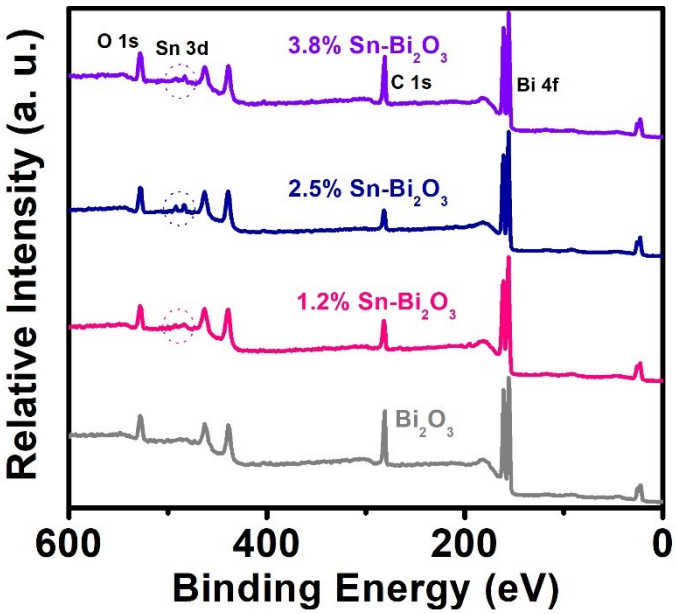

Fig. S5. The survey XPS spectra for undoped Bi_2O_3 NSs, 1.2% Sn-doped Bi_2O_3 NSs, 2.5% Sn-doped Bi_2O_3 NSs and 3.8% Sn-doped Bi_2O_3 NSs.

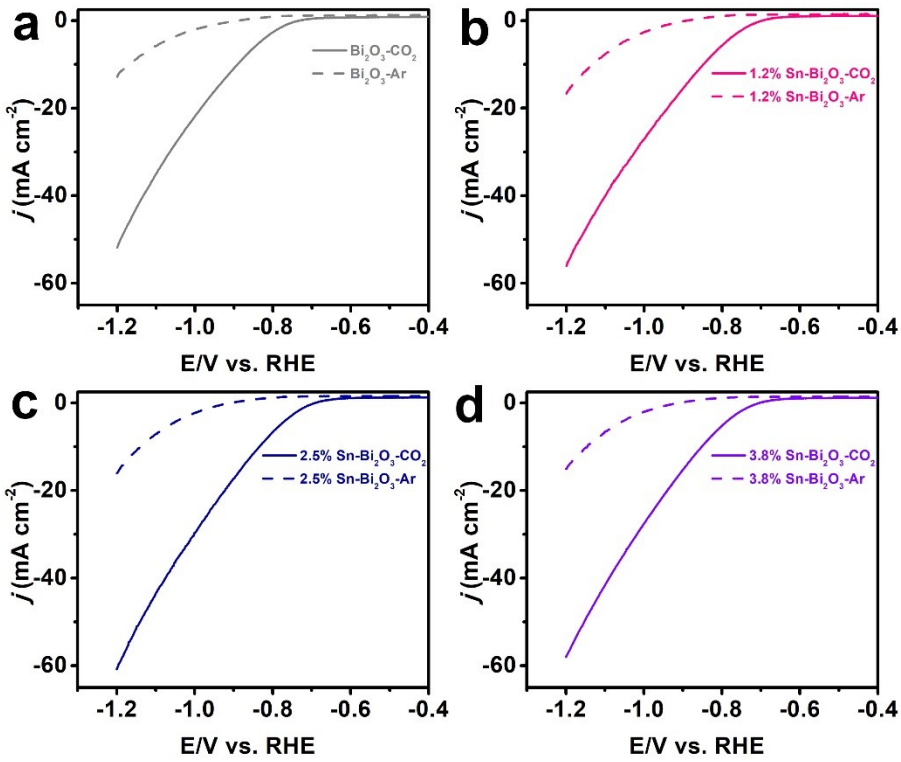

Fig. S6. Linear sweep voltammogram curves performed in Ar-saturated and CO_2-saturated 0.5M $KHCO_3$ for (a) undoped Bi_2O_3 NSs, (b) 1.2% Sn-doped Bi_2O_3 NSs, (c) 2.5% Sn-doped Bi_2O_3 NSs and (d) 3.8% Sn-doped Bi_2O_3 NSs.

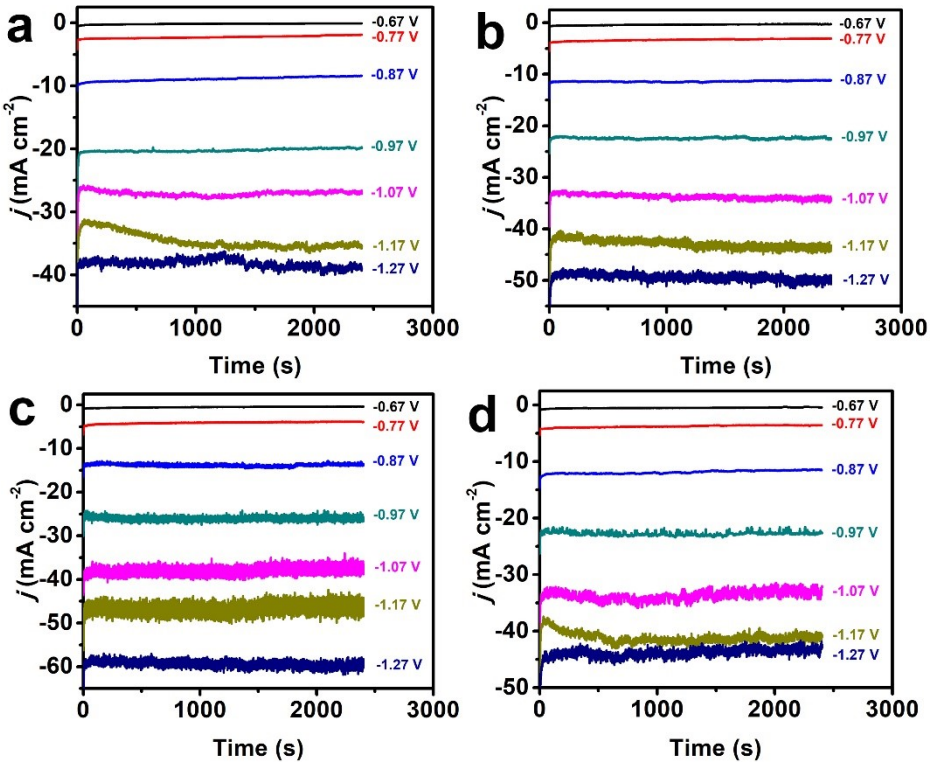

Fig. S7. Plots of current densities *j* as a function of time (chronoamperograms) during CO_2RR at different cathodic potentials for (a) undoped Bi_2O_3 NSs, (b) 1.2% Sn-doped Bi_2O_3 NSs, (c) 2.5% Sn-doped Bi_2O_3 NSs and (d) 3.8% Sn-doped Bi_2O_3 NSs.

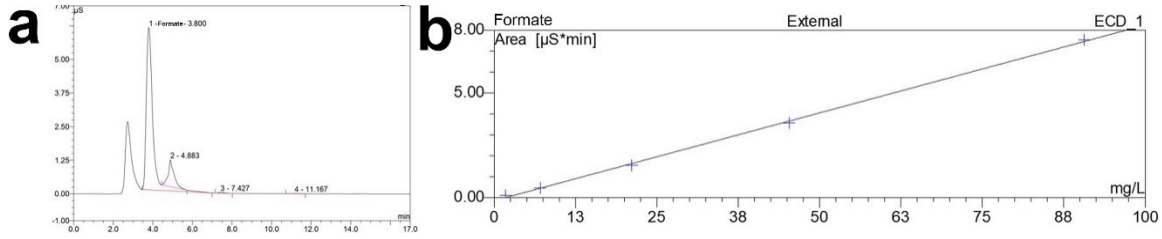

Fig. S8. (a) Ionic chromatography spectrum of the electrolyte obtained after 40 min electrolysis at -0.97 V of the 2.5% Sn-doped Bi_2O_3 NSs and (b) the standard curve of formic acid ($HCOO^-$).

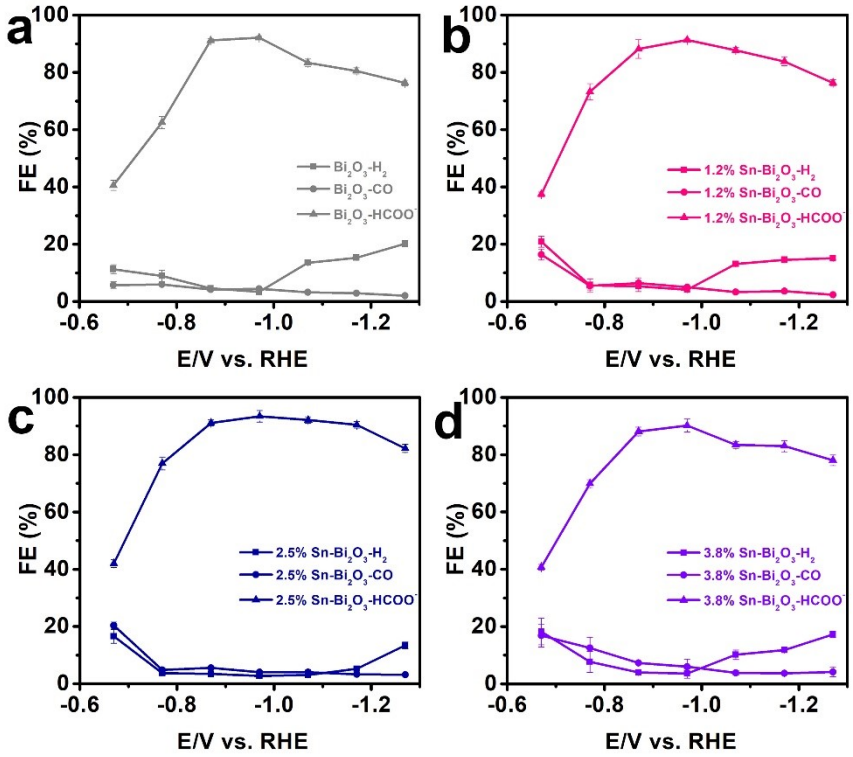

Fig. S9. Potential-dependent FEs of $HCOO^-$, CO, and H_2 for (a) undoped Bi_2O_3 NSs, (b) 1.2% Sn-doped Bi_2O_3 NSs, (c) 2.5% Sn-doped Bi_2O_3 NSs and (d) 3.8% Sn-doped Bi_2O_3 NSs.

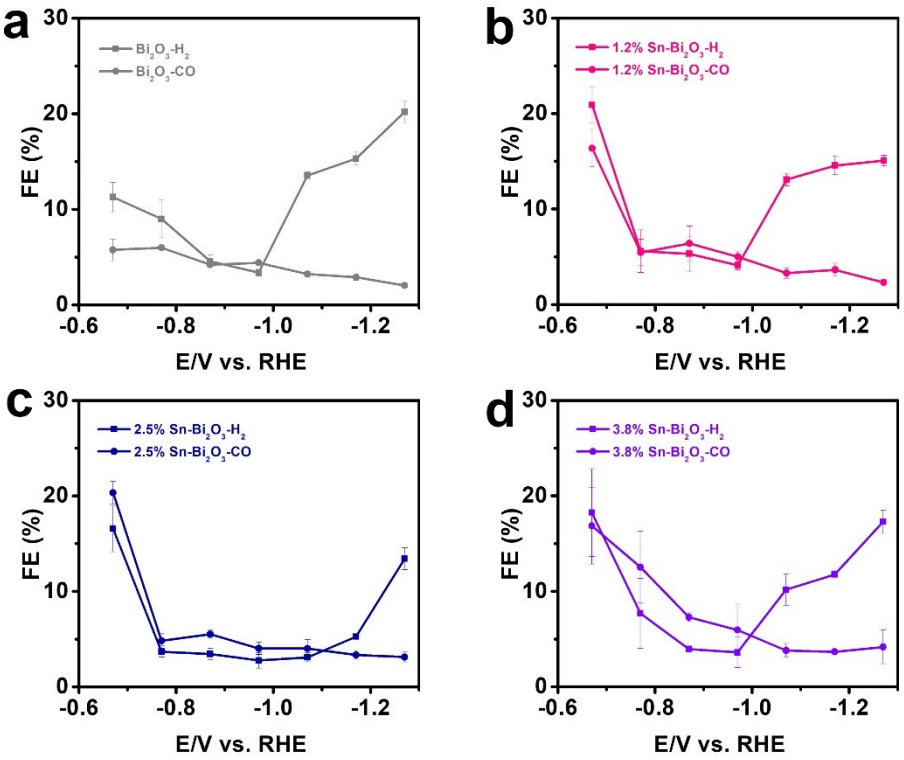

Fig. S10. Potential-dependent FEs of CO and H_2 for (a) undoped Bi_2O_3 NSs, (b) 1.2% Sn-doped Bi_2O_3 NSs, (c) 2.5% Sn-doped Bi_2O_3 NSs and (d) 3.8% Sn-doped Bi_2O_3 NSs.

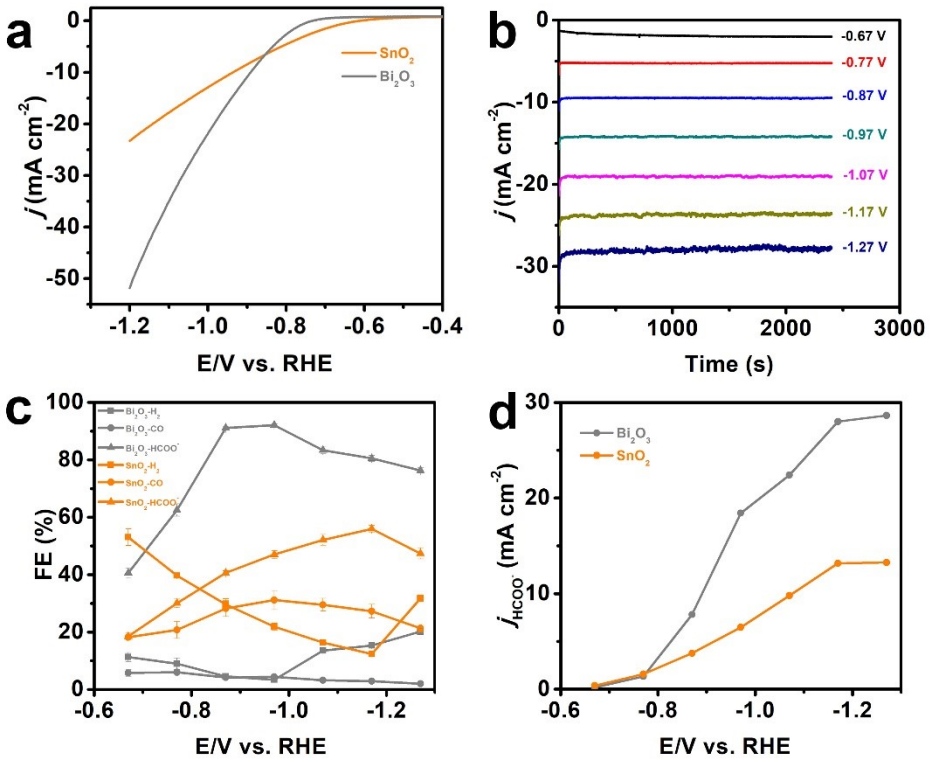

Fig. S11. (a) Linear sweep voltammogram curves performed in CO_2-saturated 0.5 M $KHCO_3$ for SnO_2 and undoped Bi_2O_3 NSs, (b) plots of current densities *j* as a function of time during CO_2RR at different cathodic potentials for SnO_2, (c) potential-dependent FEs of $HCOO^-$, CO, and H_2 for SnO_2 and undoped Bi_2O_3 NSs, and (d) formate partial current densities for SnO_2 and undoped Bi_2O_3 NSs.

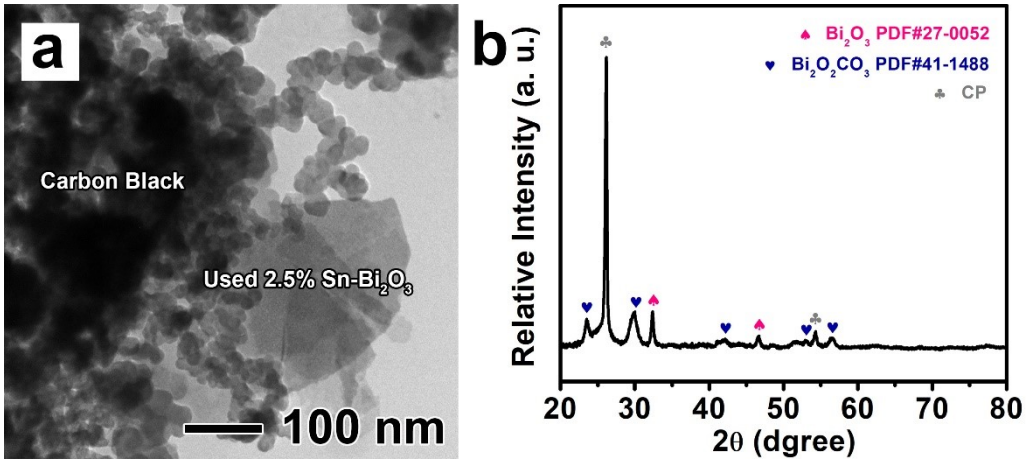

Fig. S12. (a) TEM image and (b) XRD pattern of 2.5% Sn-doped Bi_2O_3 NSs after stability test.

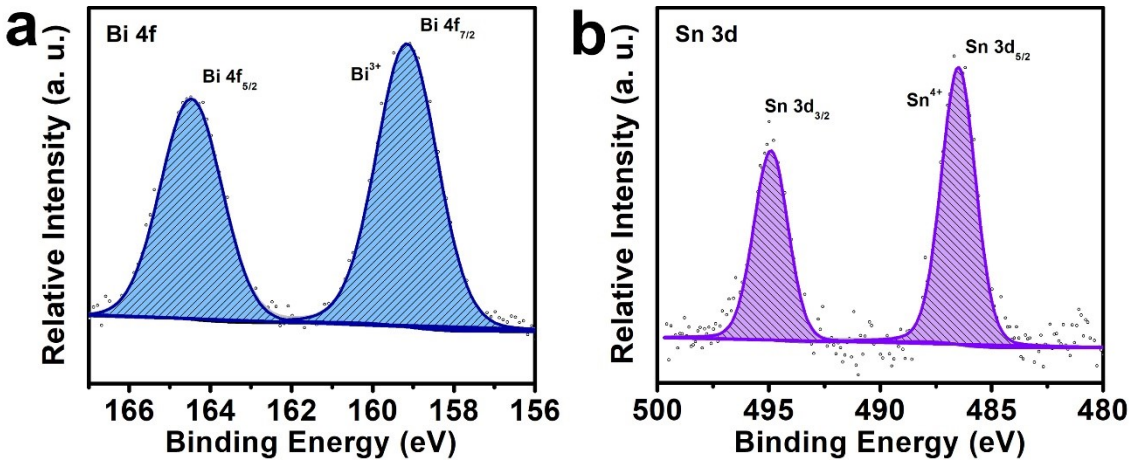

Fig. S13. XPS spectra of (a) Bi 4f orbitals and (b) Sn 3d orbitals for 2.5% Sn-doped Bi_2O_3 NSs after stability test.

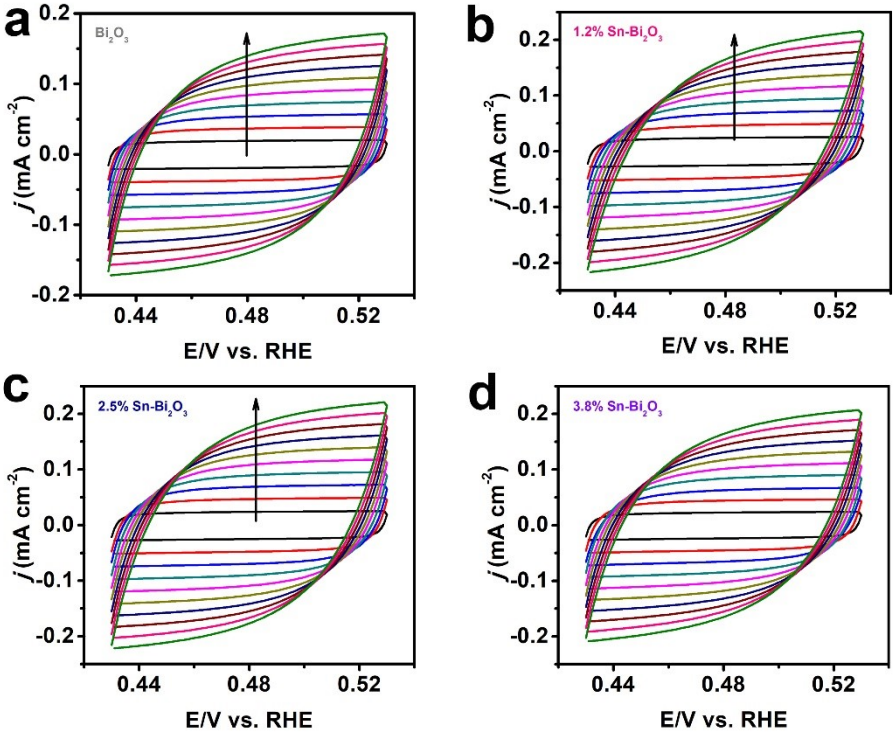

Fig. S14. Typical cyclic voltammetry curves of (a) undoped Bi_2O_3 NSs, (b) 1.2% Sn-doped Bi_2O_3 NSs, (c) 2.5% Sn-doped Bi_2O_3 NSs and (d) 3.8% Sn-doped Bi_2O_3 NSs at different scan rates (20 mV/s to 200 mV/s).

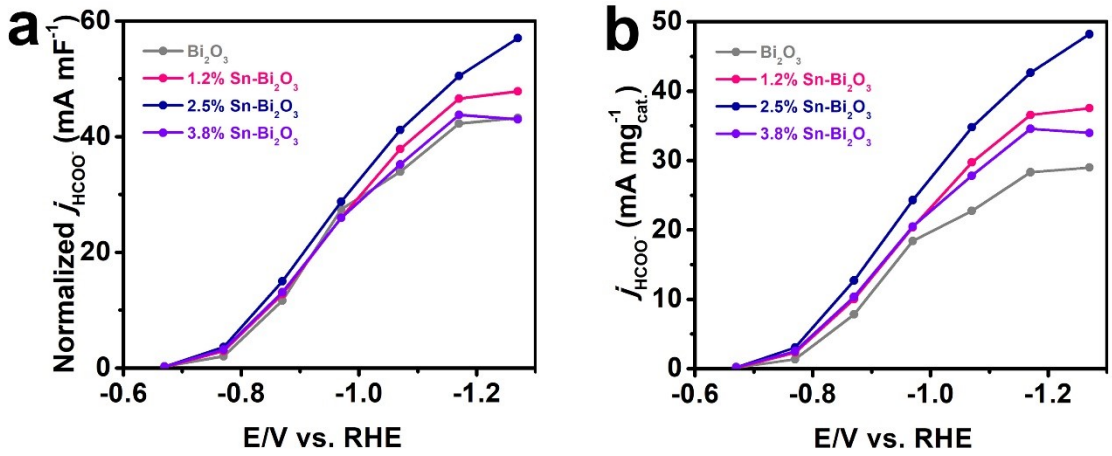

Fig. S15. (a) The j_{HCOO^-} normalized by the C_{dl} value and (b) the j_{HCOO^-} normalized by the mass for undoped Bi_2O_3 NSs, 1.2% Sn-doped Bi_2O_3 NSs, 2.5% Sn-doped Bi_2O_3 NSs and 3.8% Sn-doped Bi_2O_3 NSs.

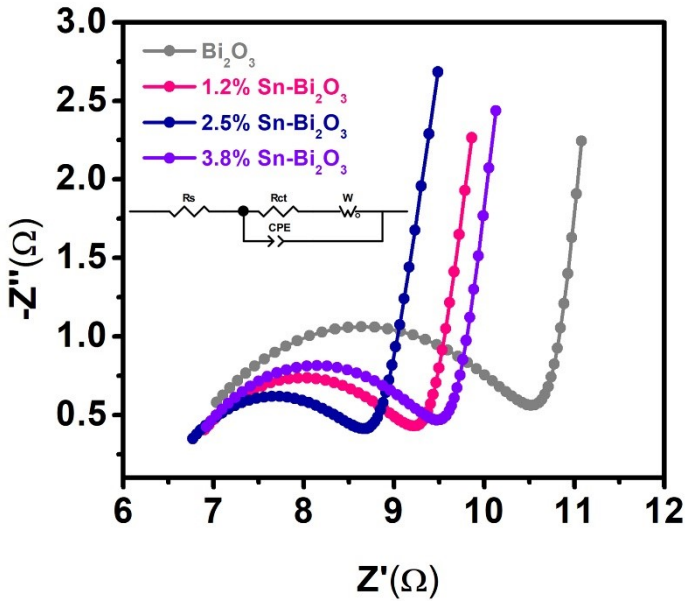

Fig. S16. Nyquist plots and the fitting equivalent circuit of undoped Bi_2O_3 NSs, 1.2% Sn-doped Bi_2O_3 NSs, 2.5% Sn-doped Bi_2O_3 NSs and 3.8% Sn-doped Bi_2O_3 NSs.

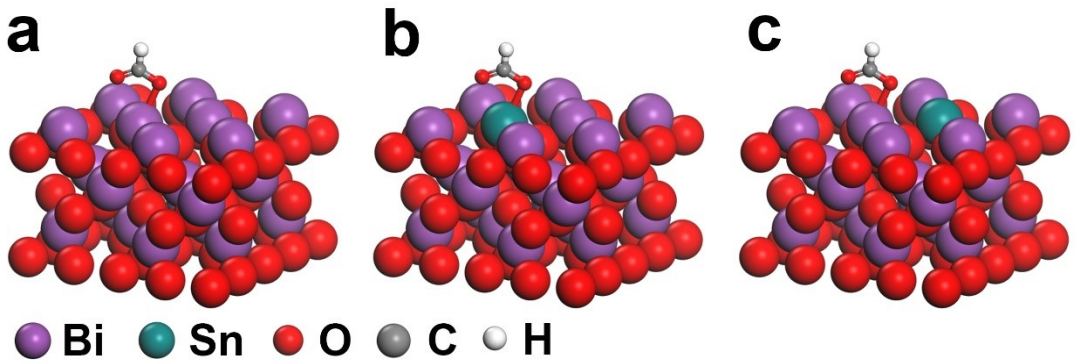

Fig. S17. DFT optimized adsorption configurations for OCHO* on (a) undoped Bi_2O_3 and (b, c) Sn-doped Bi_2O_3.

Table S1 Summarized XPS data of undoped Bi_2O_3 NSs, 1.2% Sn-doped Bi_2O_3 NSs, 2.5% Sn-doped Bi_2O_3 NSs and 3.8% Sn-doped Bi_2O_3 NSs

Samples	Bi $4f_{7/2}$	Bi $4f_{5/2}$	Sn $3d_{5/2}$	Sn $3d_{3/2}$
Undoped Bi_2O_3 NSs	159.19 eV	164.50 eV	/	/
1.2% Sn-doped Bi_2O_3 NSs	159.17 eV	164.48 eV	486.65 eV	495.06 eV
2.5% Sn-doped Bi_2O_3 NSs	159.15 eV	164.46 eV	486.69 eV	495.10 eV
3.8% Sn-doped Bi_2O_3 NSs	159.12 eV	164.43 eV	486.76 eV	495.17 eV

Table S2 Comparison of the CO_2RR activity with state-of-the-art Bi-based electrocatalysts in H-cell.

Catalyst	FE(%) @ (V vs. RHE)	Formate Current density (mA cm^{-2}) @ (V vs. RHE)	Reference
Bi_2O_3NSs@MCCM	93.8 (-1.256)	17.73 (-1.356)	[5]
Bi_2O_3NSs/NCF	94.1 (-1)	16.9 (-1)	[6]
Bi_2O_3	91 (-0.9)	8 (-0.9)	[7]
NTD-Bi	~100 (-1.05)	60 (-1.05)	[8]
Bi NS	95 (-0.87)	14.1 (-0.87)	[9]
Bi_2O_3-NGQDs	98.1 (-0.9)	18.1 (-0.9)	[10]
Bi dendrite	89 (-0.74)	2.7 (-0.74)	[11]
BiO_x/C	93.4 (-1.12)	16.1 (-1.12)	[12]
mesoporous Bi NSs	99 (-0.9)	17 (-1)	[13]
Bi NSs	86 (-1.1)	14.2 (-1.1)	[14]
Bi-MOF	92.2 (-0.9)	15 (-1.1)	[15]
Bi/Bi_2O_3	90.4 (-0.87)	38.8 (-0.87)	[16]
Bi/Bi_2O_3/NrGO	85 (-0.9)	18 (-0.9)	[17]
Bi NS	93 (-0.97)	23 (-0.97)	[18]
Bi-Sn aerogel	93.9 (-1)	9.3 (-1)	[19]
Bi-Sn/CF	96 (-1.14)	45 (-1.14)	[20]
Bi-Sn oxides	90 (CO+HCOOH) (-1)	Less than 10 (-1)	[21]
2.5% Sn-doped Bi_2O_3 NSs	**93.4 (-0.97)** **82.2 (-1.27)**	**24.3 (-0.97)** **48.2 (-1.27)**	**This work**

Table S3 The fitting values of EIS equivalent circuit

Samples	$R_s(\Omega)$	$R_{ct}(\Omega)$
Undoped Bi_2O_3 NSs	6.39	4.48
1.2% Sn-doped Bi_2O_3 NSs	6.47	2.99
2.5% Sn-doped Bi_2O_3 NSs	6.39	2.52
3.8% Sn-doped Bi_2O_3 NSs	6.49	3.25

Reference

[1] G. Kresse, J. Furthmuller, *Comp. Mater. Sci.*, 1996, **6,** 15-50.

[2] Y. Surendranath, M. W. Kanan, D. G. Nocera, *J. Am. Chem. Soc.*, 2010, **132,** 16501-16509.

[3] J. P. Perdew, K. Burke, M. Ernzerhof, *Phys. Rev. Lett.*, 1997, **78,** 1396-1396.

[4] A. A. Peterson, F. A. Pedersen, F. Studt, J. Rossmeisl, J. K. Nørskov, *Energy Environ. Sci.*, 2010, **3,** 1311.

[5] S. Liu, X. Lu, J. Xiao, X. Wang, X. Lou, *Angew. Chem. Int. Ed.*, 2019, **58,** 1-7.

[6] F. Meng, Q. Zhang, K. Liu, X. Zhang, *Chem. Eur. J.*, 2020, **26,** 4013-4018.

[7] P. Deng, H. Wang, R. Qi, J. Zhu, S. Chen, F. Yang, L. Zhou, K. Qi, H. Liu, B. Xia, *ACS Catal.*, 2020, **10,** 743-750.

[8] Q. Gong, P. Ding, M. Xu, X. Zhu, M. Wang, J. Deng, Q. Ma, N. Han, Y. Zhu, J. Lu, Z. Feng, Y. Li, W. Zhou, Y. Li, *Nat. Commun.*, 2019, **10,** 2807.

[9] N. Han, Y. Wang, H. Yang, J. Deng, J. Wu, Y. Li, Y. Li, *Nat. Commun.*, 2018, **9,** 1320.

[10] Z. Chen, K. Mou, X. Wang, L. Liu, *Angew. Chem. Int. Ed.*, 2018, **57,** 12790-12794.

[11] J. H. Koh, D. H. Won, T. Eom, N. K. Kim, K. D. Jung, H. Kim, Y. J. Hwang, B. K. Min, *ACS Catal.*, 2017, **7,** 5071-5077.

[12] C. W. Lee, J. S. Hong, K. Yang, K. Jin, J. H. Lee, H. Y. Ahn, H. Seo, N. E. Sung, K. T. Nam, *ACS Catal.*, 2018, **8,** 931-937.

[13] H. Yang, N. Han, J. Deng, J. Wu, Y. Wang, Y. Hu, P. Ding, Y. Li, Y. Li, J. Lu, *Adv. Energy Mater.*, 2018, **8,** 1801536.

[14] W. Zhang, Y. Hua, L. Ma, G. Zhu, P. Zhao, X. Xue, R. Chen, S. Yang, J. Ma, J. Liu, Z. Jin, *Nano Energy*, 2018, **53,** 808-816.

[15] F. Li, G. Gu, C. Choi, P. Kollac, S. Hong, T. Wu, Y. L. Sooe, J. Masaf, S. Mukerjeec, Y. Jung, J. Qiu, Z. Sun, *Appl. Catal. B Environ.*, 2020, **277,** 119241.

[16] D. Wu, G. Huo, W. Chen, X. Fu, J. Luo, *Appl. Catal. B Environ.*, 2020, 271, 118957.

[17] J. Sun, W. Zheng, S. L. Lyu, F. He, B. Yang, Z. Li, L. Lei, Y. Hou, *Chinese Chem. Lett.*, 2020, **31,** 1415-1421.

[18] D. Wu, X. Shen, J. Liu, C. Wang, Y. Liang, X. Fu, J. Luo, *Nanoscale*, 2019, **11,** 22125.

[19] Z. Wu, H. Wu, W. Cai, Z. Wen, B. Jia, L. Wang, W. Jin, T. Ma, *Angew. Chem. Int. Ed.*,

2021, **60,** 2-8.

[20] G. Wen, D. U. Lee, B. Ren, F. M. Hassan, G. Jiang, Z. P. Cano, J. Gostick, E. Croiset, Z. Y. Bai, L. Yang, Z. Chen, *Adv. Energy Mater.*, 2018, **8,** 1802427.

[21] J. Tian, R. Wang, M. Shen, X. Ma, H. Yao, Z. Hua, L. Zhang, *ChemSusChem*, 2021, **14,** 1-9.